Knots and Links in High Energy Physics

Masterarbeit
zur Erlangung des akademischen Grades
Master of Science

vorgelegt von
Philipp Sicking
geboren in Coesfeld

Lehrstuhl für Theoretische Physik III
Fakultät Physik
Technische Universität Dortmund
2014

1. Gutachter : Prof. Dr. Heinrich Päs

2. Gutachter : Prof. Dr. Gudrun Hiller

Datum des Einreichens der Arbeit: 30. September 2014

Abstract

This thesis analyzes two different applications for closed non-trivial topological stringlike objects arising from a Landau-Ginzburg mechanism.

A Model of determining the masses and mixing in the neutrino sector based on a Seesaw type I mechanism is introduced. The right handed neutrino mass matrix is generated by knot and link lengths. A comparison with random entries does not show a significant difference but improvements for the model are suggested.

The second part deals with a model of knotted inflation where a highly knotted network of flux tubes builds the vacuum energy, necessary for an inflationary era in the early universe. In this thesis the decay of such a network is simulated and it is shown that a phase transition similar to percolation theory occurs which indicates the end of inflation.

Contents

Chapter 1

Introduction to the Standard Model of Particle Physics

The standard model (SM) of particle physics is a well tested theory that explains the elementary particles and their behavior via a renormalizable quantum field theory. This section is based on the descriptions in [1], [2] and [3].

The SM particles are excitations of quantum fields and the interactions are generated by a local gauge symmetry

$$SU(3)_C \times SU(2)_L \times U(1)_Y \to SU(3)_C \times U(1)_{EM}, \tag{1.1}$$

where the $SU(3)_C$ indicates the strong interaction or Quantum-Chromo-Dynamics (QCD). $SU(2)_L \times U(1)_Y$ corresponds to the electroweak interaction which is spontaneously broken via the Higgs mechanism to $U(1)_{EM}$. The SM is described by the SM Lagrangian

$$\mathcal{L} = \sum_{\Psi=\{U,D,Q,L,E\}} \overline{\Psi} i \not{D} \Psi + \mathcal{L}_{Higgs} + \mathcal{L}_{Gauge} + \mathcal{L}_{Yukawa}. \tag{1.2}$$

The first term corresponds to the kinetic term of the fermions and their interaction with the gauge bosons via the covariant derivative $\not{D}$. The second one describes self-interactions of the Higgs field and the third the propagation and self-couplings of the gauge bosons. The last term is interesting for flavor physics and describes the mixing and masses of the different families. This will be discussed in detail.

The fermions are divided into quarks (Q, U and D) and leptons (L and E). Each fermion field appears in 3 different families. The well-known particle content of the

fields reads as follows:

$$Q_i = \left(\begin{pmatrix} u_L \\ d_L \end{pmatrix}, \quad \begin{pmatrix} c_L \\ s_L \end{pmatrix}, \quad \begin{pmatrix} t_L \\ b_L \end{pmatrix} \right), \tag{1.3}$$

$$L_i = \left(\begin{pmatrix} \nu_{eL} \\ e_L \end{pmatrix}, \quad \begin{pmatrix} \nu_{\mu L} \\ \mu_L \end{pmatrix}, \quad \begin{pmatrix} \nu_{\tau L} \\ \tau_L \end{pmatrix} \right), \tag{1.4}$$

$$U_i = \left(u_R, \quad c_R, \quad t_R \right), \tag{1.5}$$

$$D_i = \left(d_R, \quad s_R, \quad b_R \right) \tag{1.6}$$

$$E_i = \left(e_R, \quad \mu_R, \quad \tau_R \right). \tag{1.7}$$

The elementary matter particles are charged under the groups (1.1) as shown in table 1.1.

Field	$SU(3)_C$	$SU(2)_L$	Y
Q	3	2	$\frac{1}{6}$
U	3	1	$\frac{2}{3}$
D	3	1	$-\frac{1}{3}$
L	1	2	$-\frac{1}{2}$
E	1	1	-1

Table 1.1: Fermion fields and their representations under the gauge groups $SU(3)_C$ and $SU(2)_L$. Y denotes the hypercharge.

The quarks are triplets under $SU(3)_C$ and therefore interact via QCD due to their non-trivial color charge. The Leptons are $SU(3)_C$-singlets and thus do not interact via QCD. The weak interaction couples to the doublets under $SU(2)_L$, which are Q and L. The hypercharge $Y = Q - T_3$ can be determined through the electric Charge Q and the weak isospin T_3.

While the kinetic term and all interactions are diagonal in flavor space, the mass term in the Lagrangian is not and therefore leads to flavor physics, which describes the relation of the different generations. The basic concept of generating fermion masses is explained in the next chapter.

1.1 Fermion Masses in the Quark Sector

Since the fundamental matter particles are fermionic, they can be described by a spinor ψ and the typical mass term in the Lagrangian is

$$\mathcal{L}_{mass} = \overline{\psi} m \psi. \tag{1.8}$$

By decomposing the spinor ψ into the right and left handed parts ψ_R and ψ_L denoting the different possibilities of chirality, it is obvious to see how the mass term breaks chirality

$$\mathcal{L}_{mass} = \overline{\psi_L} m \psi_R + \overline{\psi_R} m \psi_L. \tag{1.9}$$

In the SM the fermion masses are obtained from the Yukawa Lagrangian $\mathcal{L}_{Yukawa}$. The terms related to quark masses read

$$\mathcal{L}^{Q}_{Yukawa} = -\overline{Q}_i (Y_u)_{ij} \Phi^C U_j - \overline{Q}_i (Y_d)_{ij} \Phi D_j + h.c. \,, \tag{1.10}$$

with the family indices i,j = 1,2,3 and the 3×3 complex Yukawa matrices $Y_{u,d}$. The $SU(2)_L$-doublets of the left handed particles couple to the Higgs field Φ and the right handed singlet. Φ is a scalar field and is a doublet under $SU(2)_L$ in the simplest case since the Lagrangian has to be a singlet. The Higgs doublet can be parametrized by

$$\Phi = \begin{pmatrix} \Phi^+ \\ \Phi^0 \end{pmatrix}. \tag{1.11}$$

The conjugate Higgs field is given by

$$\Phi^C = i\sigma_2 \Phi^* = \begin{pmatrix} \Phi^{0*} \\ -\Phi^- \end{pmatrix} \tag{1.12}$$

with the Pauli-matrix $\sigma_2 = \begin{pmatrix} 0 & -i \\ i & 0 \end{pmatrix}$.

The Higgs fields Φ and Φ^C give masses to the down type and up type quarks, respectively. Assuming a non vanishing vacuum expectation value $\langle \Phi^0 \rangle = \frac{v}{\sqrt{2}}$ for the Higgs field, $SU(2)_L \times U(1)_Y$ will be broken spontaneously to $U(1)_{EM}$. After this spontaneous symmetry breaking (SSB) the Yukawa Lagrangian in the quark sector reads

$$\mathcal{L}^{Q}_{Yukawa} = -\overline{u}_L Y_d \frac{v}{\sqrt{2}} u_R - \overline{d}_L Y_u \frac{v}{\sqrt{2}} d_R + h.c. \tag{1.13}$$

By identifying the factor $Y_{d,u}\frac{v}{\sqrt{2}} = M_{u,d}$ as a complex 3×3 mass matrix, the typical mass term (1.9) is obtained.

The Yukawa matrices $Y_{u,d}$ are written in their flavor basis. In general, one has to distinguish between flavor and mass eigenstates, where to obtain the latter one has to insert the unitary matrices $V^\dagger_{u,d} V_{u,d} = \mathbb{1}$ and $U^\dagger_{u,d} U_{u,d} = \mathbb{1}$.

$$\mathcal{L}_{Yukawa} = \underbrace{\overline{u_L} V_u^\dagger}_{\overline{u'_L}} \underbrace{V_u M_u U_u^\dagger}_{diag(m_u,m_c,m_t)} \underbrace{U_u u_R}_{u'_R} + \underbrace{\overline{d_L} V_d^\dagger}_{\overline{d'_L}} \underbrace{V_d M_d U_d^\dagger}_{diag(m_d,m_s,m_b)} \underbrace{U_d d_R}_{d'_R} + h.c. \tag{1.14}$$

This transformation of the fields into their mass basis does not affect the interaction with the neutral gauge bosons. That is the reason why there are no flavor-changing neutral currents on tree level in the SM. However, the interaction via charged currents does change

$$\mathcal{L} \subset \frac{g}{\sqrt{2}} W^+_\mu \overline{u_L} \gamma^\mu d_L \tag{1.15}$$

$$= \frac{g}{\sqrt{2}} W^+_\mu \overline{u'_L} \underbrace{V_u V_d^\dagger}_{V_{CKM}} \gamma^\mu d'_L. \tag{1.16}$$

The Matrix V_{CKM} determines the mixing between the different flavors via charged currents. This matrix was first proposed by Cabibbo [4] in case of 2 quark generations and then generalized by Kobayashi and Maskawa [5] to three quark generations.

In the SM V_{CKM} has to be unitary because it represents a basis transformation. The unitarity of V_{CKM} is tested to validate or falsify the SM. The entries of this mixing matrix can be measured by experiments via hadron-decays or meson-oscillations. An experimentally determined fact is the strictly hierarchical structure of V_{CKM} best seen in the Wolfenstein-parametrization [6]

$$V_{CKM} = \begin{pmatrix} 1-\frac{\lambda^2}{2} & \lambda & A\lambda^3(\rho - i\eta) \\ -\lambda & 1-\frac{\lambda^2}{2} & A\lambda^2 \\ A\lambda^3(1-\rho-i\eta) & -A\lambda^2 & 1 \end{pmatrix} + \mathcal{O}(\lambda^4) \tag{1.17}$$

with A,ρ,$\eta = \mathcal{O}(1)$ and the Wolfenstein parameter $\lambda \simeq 0.2$. As a consequence of this hierarchy the mixing between different flavors is small. We will see in the following chapter that this is not the case in the leptonic sector.

1.2 Fermion masses in the lepton sector

The general mechanism for generating fermionic masses has been outlined in the previous section. This mechanism can also be applied to the leptonic sector of the fermions.

$$\mathcal{L}_{Yukawa} \subset -\overline{L}_i (Y_l)_{ij} \Phi E_j + h.c. \underset{SSB}{\longrightarrow} -\bar{l}_L Y_l \frac{v}{\sqrt{2}} l_R + h.c. \tag{1.18}$$

Right handed neutrinos do not participate in any of the SM interactions, therefore right handed neutrinos are not part of the SM particle content. This is the reason for the absence of a corresponding neutrino mass term in the Yukawa Lagrangian and leads to massless neutrinos in the minimal SM.

However, since there is experimental evidence for nonzero neutrino masses from neutrino oscillation experiments (see chapter 1.3) the minimal SM has to be extended. In general, there are two possible ways to introduce neutrino masses depending whether neutrinos are Dirac or Majorana particles. The case of a Majorana particle is more general since a Dirac and a Majorana mass is allowed while in case of a Dirac particle the mass can only be generated by a Dirac mass term.

1.2.1 Dirac Mass

The Dirac Neutrino Mass corresponds to the mass of the charged fermions in the standard-model. Therefore one can introduce a right handed neutrino field ν_R for each generation and receive a mass term in the Lagrangian after symmetry breaking.

$$\mathcal{L}_{Dirac} = \overline{\nu_L} M_D \nu_R \tag{1.19}$$

with a complex 3×3-Matrix M_D, called Dirac mass matrix. The typical Feynman-diagram for a Dirac mass is shown in figure 1.1

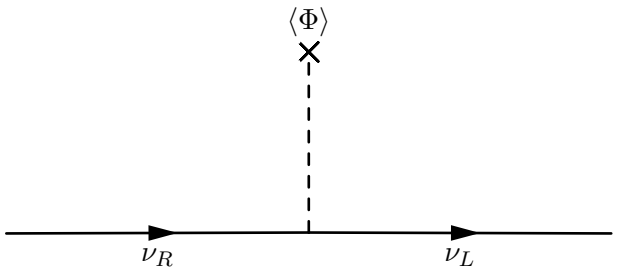

Figure 1.1: Feynman diagram for neutrino Dirac-mass.

1.2.2 Majorana Mass

The other possibility to generate neutrino masses is the so called Majorana mass. The Majorana mass can only be generated if a fermion ψ is its own anti-particle, which means

$$\psi = \psi^C = C\psi = -i\gamma^2\psi^* \tag{1.20}$$

Obviously this is only possible if the fermion has no electric charge, which is the case for neutrinos. If (1.20) holds, it is straightforward to show that the right handed field can be replaced by the left handed field

$$\psi_R = \left(\psi^C\right)_R = \left(\psi_L\right)^C. \tag{1.21}$$

In this case there is no need to introduce a new light right handed neutrino. The Majorana neutrino-mass term now can be written as

$$\mathcal{L}_{Maj} = \overline{\nu_L} M_{maj} \left(\nu_L\right)^C + \overline{\left(\nu_L\right)^C} M_{maj} \nu_L, \tag{1.22}$$

with again a complex 3×3 matrix M_{maj}, called Majorana mass matrix. As opposed to the Dirac mass matrix the Majorana mass matrix has to be symmetric.

It is easy to see that the Majorana mass term breaks lepton number L which used to be a good quantum number in the minimal standard model. Another problem is that the two left handed neutrinos form an $SU(2)$-triplet, so the Higgs doublet has to be included twice in the mass term before symmetry breaking

$$\mathcal{L}_{Maj} = \frac{1}{2}\overline{L_L^C} L_L \frac{\Phi\Phi}{M}. \tag{1.23}$$

The effective mass M needs to be introduced so that the Lagrangian still has mass dimension 4. Equation (1.23) corresponds to the Feynman diagram shown in figure 1.2. At present the Majorana type of neutrinos is not confirmed by experiments. Note that this Lagrangian is not renormalizable and can only be seen as an effective interaction. However, the term can explain the smallness of the neutrino masses. If the effective Mass M is large, the neutrino-mass will be small. An approach with a renormalizable interaction generating this term and the scenario adopted in this thesis is the Seesaw-Mechanism.

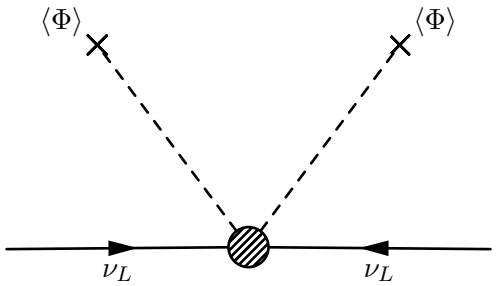

Figure 1.2: Feynman diagram for generating a neutrino Majorana mass by an effective interaction.

1.2.3 Seesaw Mechanism Type I

Consider a mass-term in the neutrino sector as follows

$$\mathcal{L}_{Mass} = \underbrace{g\langle\Phi^0\rangle}_{M_D}\overline{\nu_R}\nu_L + \frac{M_M}{2}\overline{\nu_R^C}\nu_R + h.c. \tag{1.24}$$

where the first term corresponds to a typical Dirac mass and the second to a Majorana mass term for the right handed neutrino. A Majorana mass term for the left handed neutrino is not allowed since it does not only violate lepton number conservation but also violates hypercharge conservation. Note that the mass-scale of this right handed neutrino is much larger than the electroweak scale. Since the Majorana mass term is a singlet under the SM group, it is not influenced by the breaking of the SM. Therefore the mass scale can be large, typically at the cutoff scale of the SM, e.g. the scale of a grand unified theory or the string scale. This gives room for new physics beyond the SM. The Feynman diagram for this process is shown in figure 1.3.

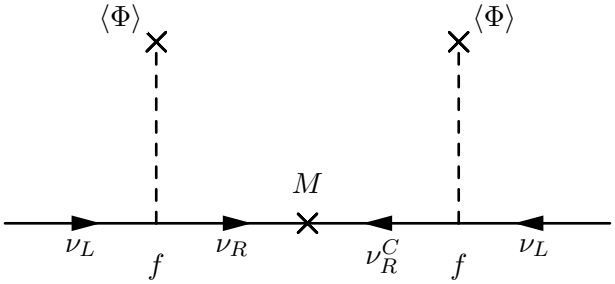

Figure 1.3: Feynman diagram for the Seesaw mechanism type I.

For an effective approach you can integrate out the heavy particle ν_R and get the effective Lagrangian

$$\mathcal{L}_{eff} = \frac{f^2}{2M_M}\langle\Phi^0\rangle\langle\Phi^0\rangle\overline{\nu_L^C}\nu_L. \tag{1.25}$$

This is exactly the term seen in (1.22). The feynman-diagram now can be seen in figure 1.4. Calculating the effective masses is equivalent to diagonalizing the matrix

$$\begin{pmatrix} 0 & M_D \\ M_D & M_M \end{pmatrix}, \tag{1.26}$$

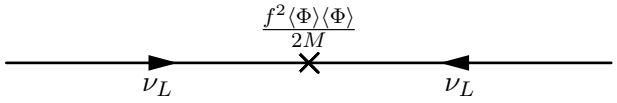

Figure 1.4: Feynman diagram for the Seesaw mechanism type I with ν_R integrated out.

yielding an effective mass of the light left handed neutrinos as

$$M_{\nu_L} \simeq \frac{m_D^2}{M_M}, \tag{1.27}$$

or for n generations, where M_D and M_M are in general complex $n \times n$ matrices,

$$M_{\nu_L} \simeq M_D^T M_M^{-1} M_D. \tag{1.28}$$

1.3 Lepton Mixing Matrix and Experimental Constraints

In analogy to the CKM-Matrix in the quark sector one can introduce the Pontecorvo–Maki–Nakagawa–Sakata (PMNS) matrix

$$U_{PMNS} = V_l^\dagger U_\nu, \tag{1.29}$$

which rotates fields from mass to flavor-space. This PMNS matrix becomes non-trivial if any neutrino mass matrix is generated, regardless of which mechanism is used as long as its structure differs from the one of the charged leptons. V_l denotes the unitary matrix which diagonalizes Y_l (see equation (1.18)) and is assumed to be $\mathbb{1}$ in this thesis, due to the fact we can choose any basis without changing the physics. U_ν is the matrix diagonalizing the neutrino mass matrix M_{ν_L} given in flavor-space so that

$$U^T M_{\nu_L} U = diag(m_1,m_2,m_3) \tag{1.30}$$

with the neutrino masses m_1, m_2 and m_3. The elements of the PMNS-matrix can be parametrized in the measured parameters of neutrino oscillation experiments.

$$U_{PMNS} = \begin{pmatrix} c_{12}c_{13} & s_{12}c_{13} & s_{13}e^{-i\delta_{CP}} \\ -s_{12}c_{23} - c_{12}s_{23}s_{13}e^{i\delta_{CP}} & c_{12}c_{23} - s_{12}s_{23}s_{13}e^{-i\delta_{CP}} & s_{23}c_{13} \\ s_{12}s_{23} - c_{12}c_{23}s_{13}e^{i\delta_{CP}} & -c_{12}s_{23} - s_{12}c_{23}s_{13}e^{-i\delta_{CP}} & c_{23}c_{13} \end{pmatrix} \cdot P \tag{1.31}$$

with $P = diag(e^{i\alpha},e^{i\beta},0)$ containing the Majorana phases and s_{ij}, c_{ij} are abbreviations for $\sin\theta_{ij}$ and $\cos\theta_{ij}$. The phase δ_{CP} is responsible for CP-violation.

Determining the elements in U_{PMNS} and the neutrino-masses m_i in experiments is rather difficult since typical neutrino cross-sections are tiny. Nevertheless there are several experiments which measure properties of the neutrino masses:

One way to identify the absolute value of the neutrino mass is by precisely measuring the tail of the energy spectrum of β decays. Since β decay ($n \to p + e^- + \bar{\nu_e}$) is a three

body decay the energy distribution of the electron is continuous and the absolute neutrino mass contributes to the cutoff in the spectrum. Current experiments determined an upper bound of $m_\nu < 2.8$ eV$(95\% C.L.)$ [7] and $m_\nu < 2.2$ eV$(95\% C.L.)$ [8].

Another approach is to search for neutrinoless double beta-decays, as done by the GERDA-experiment. Finding such an neutrinoless double beta decay would prove that neutrinos are Majorana particles and give access to the (1,1)-element in the neutrino mass matrix. A range for an upper limit on $m_{\beta\beta} = \sum_i U_{ei}^2 m_i$ of $0.2 - 0.4$eV is given by [9] .

The sum of the neutrino masses has much influence on cosmological observations e.g., the formation of structures in the universe and primordial nucleosynthesis. The current constraint is $\sum_i m_i < 0.23$eV [10].

To get access to the parameters in the mixing matrix and the mass squared differences $\delta m_{ij}^2 = m_i^2 - m_j^2$, neutrino oscillations are analyzed. Neutrino oscillation is the conversion of a neutrino from one flavor eigenstate to another and back with respect to the travel distance. Since the flavor eigenstates and mass eigenstates mismatch, the probability of measuring a neutrino, produced as an electron neutrino, as an electron neutrino after travel distance L is

$$P_{\nu_e \to \nu_e} = 1 - \sum_{i,j} 4|U_{ei}|^2 |U_{ej}|^2 \sin^2 \frac{\delta m_{ij}^2}{4E} L \tag{1.32}$$

with the neutrino energy E.

Measuring the neutrino flux at different distances yields information about δm_{ij}^2 and the mixing angles θ_{ij}. As already known neutrino masses are small, and so are the squared differences. Therefore, to be sensitive to small δm^2, the energy has to be low (reactor experiments) or the baseline has to be long (accelerator experiments). But not only artificial neutrino sources are used to determine the mixing parameters but also atmospheric neutrinos and solar neutrinos. Several experiments currently measure neutrino oscillations like DOUBLE CHOOZ, DAYA BAY, RENO (all reactor experiments), KamLAND (reactor and long baseline experiment), T2K, MINOS, CNGS (all long baseline experiments) or Super-Kamiokande (atmospheric and solar neutrinos). A current global fit to all recent data gives best fit values for each parameter with 1σ-uncertainty [11]

$$\sin^2 \theta_{12} = 0.302^{+0.013}_{-0.012}, \tag{1.33}$$
$$\sin^2 \theta_{23} = 0.413^{+0.037}_{-0.025}(\text{NH}), \tag{1.34}$$
$$\sin^2 \theta_{23} = 0.594^{+0.021}_{-0.022}(\text{IH}), \tag{1.35}$$
$$\sin^2 \theta_{13} = 0.0227^{+0.0023}_{-0.0024}, \tag{1.36}$$
$$\delta m_{21}^2 = 7.50^{+0.18}_{-0.19} \cdot 10^{-5}\text{eV}^2, \tag{1.37}$$
$$\delta m_{31}^2 = +2.473^{+0.70}_{-0.67} \cdot 10^{-3}\text{eV}^2(\text{NH}), \tag{1.38}$$
$$\delta m_{32}^2 = -2.427^{+0.042}_{-0.065} \cdot 10^{-3}\text{eV}^2(\text{IH}), \tag{1.39}$$
$$\delta_{CP} = 300^{+66}_{-138}\ ^\circ. \tag{1.40}$$

Note that since the squared differences are measured, only two mass differences are independent. Neutrino-oscillations cannot make any statement about the absolute mass scale. Normal hierarchy (NH) and inverse hierarchy (IH) are possible and cannot be distinguished by current oscillation experiments. For illustration of the hierarchies see figure 1.5.

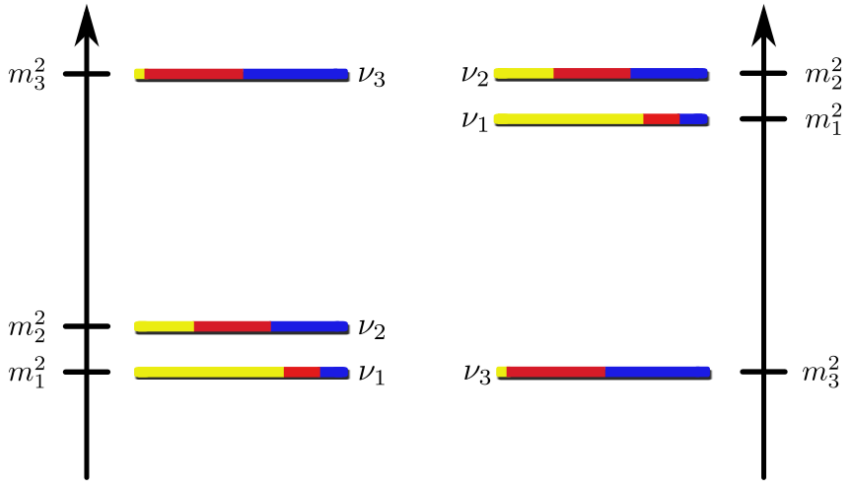

Figure 1.5: Neutrino mass hierarchy, taken from [12].

If the absolute masses are large compared to the differences, the neutrino masses are (called) degenerate.

Chapter 2

Closed Flux tubes as Knots and Links

The question why we have only three large space dimensions is not answered satisfactorily, because quantum field theories can easily be extended to more than three spacial dimensions. It can be proposed that the reason for exactly three spacial dimensions lies in the special properties of a three dimensional space. One approach is to look at the mathematical topic of knot theory. It is a subtopic of topology and is defined on $\mathbb{R}^3$ (see chapter 2.1).

If knots have to be realized in a physical context this is only possible in three spatial dimensions. One might also consider the other side of the argument: Knots can only be realized physically because there are three space dimensions. Knot like structures in a high energy context can arise in a Landau Ginzburg Model where flux tubes form string like objects which can be treated as knots (see 2.3).

The chapters 3 and 4 discuss two concrete applications of knot like structures, which might be improvements to the SM. The first is a possibility of right handed neutrinos at a high mass scale which are realized by closed flux tubes. This would lead to an extension of the SM explaining neutrino masses and mixing. The second one tries to model cosmological inflation and especially its end phase by a network of flux tubes during a phase transition. The decay of this network will be simulated.

2.1 Mathematical basics in Knot-Theory

First it has to be defined what a knot is in the mathematical context. A knot K is defined as the image of the homeomorphism of the unit circle C from the $\mathbb{R}^2$ -plane to $\mathbb{R}^3$. One can imagine this definition by taking a rope and splicing the ends together after perhaps winding it up.

The simplest knot is the trivial unknotted circle with $x^2 + y^2 = 1$ and $z = 0$ (see fig 2.1). The simplest non-trivial knot is the trefoil shown in figure 2.3. If two or more knots are connected so that they cannot be separated without cutting one of the knots, this object is called a link. Figure 2.2 shows the simplest link consisting of two connected

trivial knots, named Hopf-Link. From now on both knots and links are referred to as knots for simplicity.

To distinguish between different knots it is useful to classify knots into different types. Two knots are of the same type if there exists an isotopy to transform one into the other. Simply speaking, an isotopy can be imaged as deforming and twisting the knot without cutting the rope. If two knots are of the same type, they are called equivalent. For the trivial and trefoil knot it is easy to see that they are not equivalent, but for more complex knots most of the time it is not obvious. If one extends these knots to a space with more than three spatial coordinates, all knots are equivalent since one can unknot every knot by using a fourth dimension. Therefore the formation of knots is a specialty of the $\mathbb{R}^3$.

By projecting a knot into a plane, one can define its order O. This is the minimal possible number of crossings by adjusting the projecting plane.

To classify knots recent research has tried to find so called knot invariants. These allow to distinguish between different classes of knots, since knots of the same type have the same invariants. Even measures which are not different (or not proven to be different) for all types are often called knot invariants, e.g. Jones-Polynomial or tricolorability. One physical knot invariant is the knotlength following in the next section. For a further introduction to knot theory see [13].

2.2 Knotlength

The most physical approach to classify knots is the minimal ropelength of the knot, called the knotlength. The ropelength $Rop(\gamma)$ of a curve γ is defined as the fraction

$$Rop(\gamma) = \frac{Len(\gamma)}{Thi(\gamma)} \tag{2.1}$$

where $Len(\gamma)$ is the length and $Thi(\gamma)$ is the Thickness of γ (see [14] for mathematical details). Therefore the knotlength of a knot K is the minimal length of a rope with thickness 1 with which the knot K can be knotted. An analytic way for calculating the knotlength for a given knot has not been found yet but numeric calculations give access to very good approximations of the knotlength.

In Table 2.1 the knotlength of knots and links up to order 7 are shown. The Knots are written in Rolfsen-Notation O_i^l where O denotes the order. The index i counts the different types with the same order and l defines the number of knots which are linked together. In case of a missing l the object consist only out of a single knot.

Note that especially for higher crossing numbers the knotlengths are nearly degenerate. This feature lies in the fact, that the knotlength grows linearly with the crossing number but the number of possible different knots grows faster than exponentially with increasing crossing number. This degeneracy will be used in section 3.

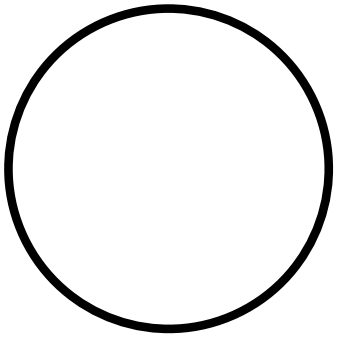

Figure 2.1: Trivial Knot

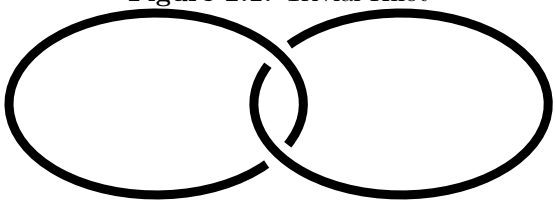

Figure 2.2: Hopf-Link

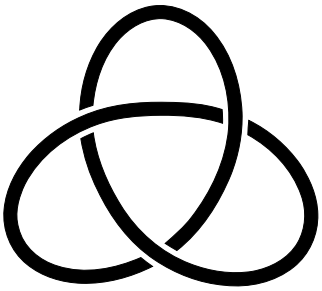

Figure 2.3: Trefoil Knot

2.3 Realization in a Quantum Field Theory

One application of knots as a mathematical object in the field of high energy-physics can be found in the formation of string-like flux tubes in abelian gauge theories. The basic concept and derivation is shown in the lecture-notes of [15], on which this chapter is based on.

The behavior and formation of flux tubes can be seen in the Landau-Ginzburg-Model, or sometimes Abelian-Higgs-Model. Consider a Lagrangian given by

$$\mathcal{L}_{LG} = -\frac{1}{4}\overline{F}_{\mu\nu}\overline{F}^{\mu\nu} + \frac{1}{2}(D_\mu\phi)(D^\mu\phi)^\dagger - \frac{\lambda}{2}(\phi\phi^* - v^2)^2, \tag{2.2}$$

with a complex scalar-field ϕ and the dual field tensor $\overline{F}^{\mu\nu}$. $D_\mu = \partial_\mu + igB_\mu$ denotes the covariant derivative with the vector potential B^μ. The field ϕ represents a (chromo-)

Knot	Knotlength	Index	Link	Linklength	Index
3_1	32.7436	00	2_1^2	25.1334	01
4_1	42.0887	01	4_1^2	40.0122	02
5_1	47.2016	02	5_1^2	49.7716	03
5_2	49.4701	03	6_1^2	54.3768	04
6_1	56.7058	04	6_2^2	56.7000	05
6_2	57.0235	05	6_3^2	58.1013	06
6_3	57.8392	06	6_1^3	57.8141	07
7_1	61.5067	07	6_2^3	58.0070	08
7_2	63.8556	08	6_3^3	50.5539	09
7_3	63.9285	09	7_1^2	64.2345	10
7_4	64.2687	10	7_7^2	65.0204	11
7_5	65.2560	11	7_3^2	65.3257	12
7_6	65.6924	12	7_4^2	65.0602	13
7_7	65.6086	13	7_5^2	66.1915	14
			7_6^2	66.3147	15
			7_7^2	55.5095	16
			7_8^2	57.7631	17
			7_1^3	65.8062	18

Table 2.1: Length of Knots and Links up to order seven [14]. The column Index refers to the numeration used in chapter 3.

magnetic charge condensate with the magnetic charge g. The underlying gauge group is not important at this point, but may be a picture describing the confinement of QCD.

This model is called "dual superconductor", because the electric and magnetic charges and currents are exchanged, so that the theory is described by the magnetic charges and currents instead of the electric ones. To take electric charges into account, one has to add a string term $\overline{G}_{\mu\nu}$, similar to the description of Dirac-Strings.

$$\overline{F}_{\mu\nu} = (\partial_\mu B_\nu - \partial_\nu B_\mu) + \overline{G}_{\mu\nu} \tag{2.3}$$

The last term in (2.2) denotes the potential for ϕ and gives the non-zero vacuum expectation value $\phi\phi^* = v^2 \neq 0$ for lower energies. This gives rise to two different phases before and after SSB in analogy to the Higgs-Mechanism in the SM. The first phase, with $\phi\phi^* = v^2$, is the superconductive or color-confined-phase, the other phase with $\phi\phi^* = 0$ is the normal phase in which QCD is asymptotically free. This is very similar to the normal superconductive picture.

In a superconductor, there is no magnetic field due to the Meissner-Ochsenfeld-effect. Similarly, in the dual superconductive picture there is no electric field, if the system is in the superconductive phase. In QCD electric charges exist, e.g. quarks, which play the role as magnetic monopoles do in case of Dirac strings. The Meissner-Ochsenfeld-effect cannot avoid chromo-electric currents entirely but pushes them into a string like object, the flux tube.

Similar to the Higgs mechanism in the SM, the phase transition gives rise to a nonzero Higgs-Mass $m_H = 2v\lambda$ and the mass for the gauge field $m_V = gv$. This corresponds to the typical superconductor properties, the penetration depth $\frac{1}{m_V}$ and the correlation length $\frac{1}{m_H}$. The first is the distance after which the chromo-electric-field vanishes outside the flux tubes ("thickness" of the tube). The latter corresponds to the distance in which the scalar field acquires its vacuum expectation value.

For long flux tubes it can be shown that the energy of a flux tube is proportional to the distance R between the chromo-electric charges, or the length of the flux tubes

$$E = \sigma R. \tag{2.4}$$

with the string tension σ. For further details see [15]. Equation (2.4) is the typical linear potential of QCD in confinement.

All these phenomena can also occur in other (non-) abelian gauge theories. In this thesis we do not concentrate on the mechanisms of forming such flux tubes, but discuss two different kinds of phenomena, which might provide an application for closed flux tubes. In case of transition from a normal to a dual superconducting phase with a huge number of (chromo-) electric charges, the generation of numerous flux tubes is likely, which can be closed as well. Due to the fact that energy is minimized, these flux tubes will tighten up and can be treated as knots.

Chapter 3

Determining Lepton Flavor via Knotlength

3.1 Generating Neutrino Masses

As pointed out in chapter 1.3 the mixing matrix in the leptonic sector differs from the one in the quark sector. The mixing is large and the neutrino masses are small. Therefore, the hierarchical structure in the CKM-Matrix cannot be reproduced in the PMNS-Matrix. These differences in the experimental data may correspond to the peculiarities of generating neutrino masses.

In chapter 1.2 the different mechanisms to generate neutrino masses are introduced, and it is shown that a seesaw-like mechanism is an attractive way to explain the smallness of the neutrino masses. The model used in this thesis is based on [16] and [17]. The basic idea is that the Dirac mass matrix is analogous to the mass matrices of the quarks and provides only small mixing angles. The large mixing angles observed in the leptonic sector arise from the right handed Majorana masses. For simplification we therefore assume a diagonal Dirac mass matrix

$$M_D = diag(m_1^D, m_2^D, m_3^D), \tag{3.1}$$

and a real Majorana mass matrix M_{maj} for the right handed sector since the CP-violating phase δ_{CP} in the neutrino sector is not determined sufficiently yet (see equation (1.40)).

$$M_{maj} = \begin{pmatrix} m_1^K & m_1^L & m_2^L \\ m_1^L & m_2^K & m_3^L \\ m_2^L & m_3^L & m_3^K \end{pmatrix}. \tag{3.2}$$

The entries $m_i^{K/L}$ are real parameters at the moment and will be determined in equation (3.3).

To calculate the mass-matrix of the three light left-handed neutrinos we use equation (1.28) and obtain

$$M_{\nu_L} = \frac{1}{\Delta^3}\begin{pmatrix} [m_2^K m_3^K - (m_3^L)^2](m_1^D)^2 & (m_2^L m_3^L - m_3^K m_1^L)m_1^D m_2^D & (m_1^L m_3^L - m_2^K m_2^L)m_1^D m_3^D \\ (m_2^L m_3^L - m_3^K m_1^L)m1^D m_2^D & [m_1^K m_3^K - (m_2^L)^2](m_2^D)^2 & (m_1^L m_2^L - m_1^K m_3^L)m_2^D m_3^D \\ (m_1^L m_3^L - m_2^K m_2^L)m_1^D m_3^D & (m_1^L m_2^L - m_1^K m_3^L)m_2^D m_3^D & [m_1^K m_2^K - (m_1^L)^2](m_3^D)^2 \end{pmatrix}, \quad (3.3)$$

with the factor

$$\Delta^3 = -m_2^K (m_1^L)^2 + 2m_1^L m_2^L m_2^L - m_2^K (m_2^L)^2 - m_1^K (m_3^L)^2 + m_1^K m_2^K m_2^K. \quad (3.4)$$

Before the measurement of $\theta_{13} \neq 0$, a good approximation of the leptonic mixing matrix was given by the tribimaximal scheme

$$U_{TBM} = \begin{pmatrix} \sqrt{\frac{2}{3}} & \frac{1}{\sqrt{3}} & 0 \\ -\frac{1}{\sqrt{6}} & \frac{1}{\sqrt{3}} & -\frac{1}{\sqrt{2}} \\ -\frac{1}{\sqrt{6}} & \frac{1}{\sqrt{3}} & \frac{1}{\sqrt{2}} \end{pmatrix} \quad (3.5)$$

This corresponds to $\sin^2\theta_{12} = \frac{1}{3}$, $\sin^2\theta_{23} = 0.5$, $\sin^2\theta_{13} = 0$. The name arises from the tri-maximal mixing of the mass eigenstate ν_2 and the bi-maximal mixing of the mass eigenstate ν_3. This scheme is still a popular choice for model building, since the structure could give information about an underlying symmetry. Comparing these values to the current global best fits (see equation (1.33) - (1.35)), the deviations are small enough to consider them as perturbations.

It is shown in [18] that as typical mass-matrix generating such a tribimaximal mixing can be parametrized by

$$M_\nu^{TBM} = \begin{pmatrix} x & y & y \\ y & x+v & y-v \\ y & y-v & x+v \end{pmatrix}. \quad (3.6)$$

The two possible hierarchies introduced in chapter 1.3 can be realized by approximating the small mass squared difference to zero. The arising mass structures in mass basis read $diag(0,0,\tilde{m})$ for normal and $diag(\tilde{m},\tilde{m},0)$ for inverse hierarchy with the absolute non vanishing neutrino mass $\tilde{m}$. Assuming tribimaximal mixing, this corresponds to

$$M_\nu^{NH} = \tilde{m}\begin{pmatrix} 0 & 0 & 0 \\ 0 & \frac{1}{2} & -\frac{1}{2} \\ 0 & -\frac{1}{2} & \frac{1}{2} \end{pmatrix} \quad (3.7)$$

for normal hierarchy. Comparing this matrix to (3.3) leads to five relations between the

entries of the mass-matrices:

$$\frac{m_3^K}{m_2^K} = \frac{(m_2^D)^2}{(m_3^D)^2}, \tag{3.8}$$

$$\frac{m_2^L}{m_1^L} = \frac{m_3^D}{m_2^D}, \tag{3.9}$$

$$m_2^K m_2^L = m_1^L m_3^L, \tag{3.10}$$

$$m_1^K m_2^K \neq (m_1^L)^2, \tag{3.11}$$

$$\tilde{m} = 2(m_3^D)^2 \frac{(m_1^L)^2 - m_1^K m_2^K}{\Delta^3}. \tag{3.12}$$

If one assumes the Dirac masses m_i^D to be roughly equal, these relations can be solved simultaneously by an almost degenerate spectrum of m_i^L and m_i^K.

For inverse hierarchy the corresponding mass matrix in flavor space looks like

$$M_\nu^{IH} = \tilde{m} \begin{pmatrix} 1 & 0 & 0 \\ 0 & \frac{1}{2} & \frac{1}{2} \\ 0 & \frac{1}{2} & \frac{1}{2} \end{pmatrix}. \tag{3.13}$$

comparing with (3.3) and solving all resulting relations simultaneously, leads to either vanishing absolute neutrino mass $\tilde{m} = 0$ or vanishing elements in M_{maj}: $m_1^L = m_2^L = 0$ in contradiction to the assumption made above.

Based on the normal hierarchy case, the idea in [17] and for this chapter of this thesis is to combine the assumptions of almost degenerate entries in M_{Maj} with the almost degenerate knotlengths seen in Table 2.1. Since the energy of a closed flux tube is proportional to its length, a mass matrix produced by closed tight knots should be proportional to the knotlength $l_i^{K/L}$, where i denotes the index from 2.1 and the superscripts indicates whether it is a single knot (K) or a link (L). Hence the entries of M_{Maj} are generated by

$$m_i^{K/L} = l_i^{K/L} \cdot m_s \tag{3.14}$$

with an overall scale factor m_s. This scale factor determines the scale of confinement at which the new phenomena occur. For the numerical analysis this value is fixed to $m_s = 10^{12}$GeV, which is motivated by cosmological constraints (see [17] for details).

If the assumptions made above do apply, we will expect substantially more viable fits for the normal hierarchy by using the knot-spectrum for entries in the Majorana mass matrix instead of using only randomly generated entries. Furthermore the number of viable fits should be less and the goodness of fit should be worse in the case of inverse hierarchy.

These calculations have been performed already in [17] but based on older experimental data, which did not exclude $\theta_{13} = 0$. The tribimaximal mixing was therefore well motivated. The analysis seemed to confirm the expectations. In this thesis we will examine whether current data with a nonzero θ_{13} confirm the previous results.

3.2 Numerical Calculations

The algorithm for fitting the Dirac mass matrices to the experimental data works as follows. Every combination of knots and links from Table 2.1 is calculated separately. For each combination, the matrix M_{ν_L} is derived with the three arbitrary parameters m_i^D. After that the mixing matrix is calculated by diagonalizing the generated matrix with the Basic Linear Algebra Subprograms published in the GNU Scientific Library [19]. From this mixing matrix the mass squared differences and the mixing angles can be extracted. A problem is to order the mass eigenstates correctly, so that the correct mixing angles are extracted.

A χ^2 fit is applied to the experimental values from (1.33) - (1.39). This χ^2 is minimized by varying the Dirac masses m_i^D. The asymmetric errors are handled as shown in [20]. The minimization method used in this simulation is based on the Simplex algorithm [21], implemented in the GNU Scientific Library [19]. Since there are five observables and three fitting parameters, there are two degrees of freedom and for a P value of 0.01 all combinations with $\chi^2 < 9.21$ are considered viable.

To make useful statements about this model, we have to compare it with random entries in M_{maj}. Therefore 1,000,000 different variations of random numbers ranging from 0 up to the biggest knotlength are inserted in the Majorana mass matrix. For every combination the Dirac masses are adjusted to minimize the resulting χ^2.

The scan is separated into two different programs, one for normal hierarchy and one for inverse hierarchy, to ensure the correct matching of mass eigenstates. The best fits are shown in Table 3.1 for normal and in Table 3.2 for inverse hierarchy. The used indices are the same as in Table 2.1 where the corresponding knotlengths are shown.

Table 3.3 also shows the ratio of all tested models that are considered viable. For normal hierarchy, no excess is observed for models with degenerate knotlengths compared to random entries. The best fits moreover do not lead to a smaller χ^2 in comparison to random matrix-entries. For inverse hierarchy the models with degenerate knotlengths lead to a number of viable fits twice as high compared to the case of random entries but in the same range as both models of normal hierarchy. The best fits lead to a smaller χ^2 but do not make much differences in that regime.

On a closer look at the results of normal hierarchy, even the best fits in Table 3.1 do not seem to have any structure. Some of the knotlength are degenerate, which can be accidental since degeneracy always occurs in some elements of the matrix. In contradiction to the assumption made above, the Dirac masses are not degenerate in the best fits. This assumption is not well motivated if one considers the Dirac mass matrix in the neutrino sector to be analogous to the one in the charged fermion sector. There, hierarchical structures exist with non degenerate masses.

Dropping the assumption of almost degenerate Dirac-masses, the equations (3.8)-(3.11) can as well be solved by arbitrary entries in the Majorana mass matrix. Since the Dirac masses are not fixed in any way but used to minimize the χ^2, there is no motivation for assuming them to be almost equal. Moreover, even if the knot spectrum is used, the best fits do not lead to a degenerate spectrum of m_i^D.

For inverse hierarchy a structure in the best fits can also not be seen. The deviation

of the knotted spectrum to the random entries can not be seen in any analytical context and is maybe caused by accidentally well fitting numbers.

These differences to [17] may be caused by the deviation from tribimaximal mixing since $\theta_{13} \neq 0$. If this is the case, the method used for this thesis should give the same results if the same data input is used. This is part of the next section.

χ^2	K_1	K_2	K_3	L_1	L_2	L_3	m_1^D[GeV]	m_2^D[GeV]	m_3^D[GeV]
< 0.001	10	08	03	00	01	11	14.854	26.804	23.429
0.001	00	06	08	04	02	07	5.619	20.766	14.507
0.001	01	05	12	17	16	05	6.719	22.106	15.537
0.001	05	09	02	03	01	07	7.052	12.017	18.513
0.002	01	05	13	13	06	07	6.782	22.371	15.698
0.002	06	01	10	06	09	08	5.819	13.022	11.328
0.002	06	01	10	16	09	08	5.808	12.999	11.283
0.002	10	09	12	00	01	08	14.624	24.501	23.816
0.002	11	10	13	00	01	08	14.838	24.612	23.974
0.002	13	05	09	01	15	10	10.251	19.688	18.378

Table 3.1: The 10 best fits for normal hierarchy.

χ^2	K_1	K_2	K_3	L_1	L_2	L_3	m_1^D[GeV]	m_2^D[GeV]	m_3^D[GeV]
< 0.001	13	03	09	02	09	04	34.579	6.435	8.888
0.001	05	13	03	05	01	06	40.954	9.978	10.457
0.002	02	05	12	00	04	09	54.144	16.699	22.279
0.002	04	13	07	15	00	14	58.051	17.374	20.188
0.002	07	06	11	00	11	12	64.531	18.358	24.335
0.002	11	09	03	01	04	07	56.507	14.207	15.356
0.002	12	01	07	05	09	08	33.176	4.922	7.169
0.002	13	05	12	15	00	09	64.227	17.061	21.994
0.003	12	08	13	02	10	17	45.718	10.363	12.825
0.003	12	08	13	02	12	17	45.756	10.372	12.847

Table 3.2: The 10 best fits for inverse hierarchy.

3.3 Comparison with former analysis

The best fits using the experimental values as used in [17] (see equations (A.1)-(A.6)) are shown in Tables A.1 and A.2 for normal hierarchy and inverse hierarchy, respectively. A comparison to random numbers in the Majorana mass matrix is given in Table A.3. The best fits proposed in [17] can not be found and a substantial deviation between knotlength and random entries does not occur either.

Model	tested parameters	viable fits	ratio viable fits	$\chi^2_{bestfit}$
NHknots	10,692,864	33,863	0.317%	< 0.001
NHrandom	1,000,000	3,369	0.337%	0.004
IHknots	10,692,864	35,044	0.328%	< 0.001
IHrandom	1,000,000	1,458	0.146%	0.008

Table 3.3: Number of viable fits for the different models.

On a closer look at the best fit in [17] and by calculating the mixing, it is easy to see that these entries lead to a wrong mixing scheme. Compared to Figure 1.5 the mass eigenstates m_1 and m_2 are exchanged. Therefore there has to be a mistake in the past analysis.

3.4 Interpretation of the Results

The method of scanning introduced above needs a justification. In the universe we see, the mixing in the leptonic sector is described by the experimental data (see equations (1.33) - (1.40)). It is obvious that only one special underlying mass matrix generates this mixing scheme and therefore only one special combination of entries in the mass matrix has to reproduce the experimental data.

If the model of knotlength determining the right handed mass matrix describes nature appropriately, one combination of knots is realized in this universe. The number of different combinations by which the experimental data can be reproduced, does not say anything about the correctness of the model. However, it is possible to say if such a mixing scheme is somewhat special or more a regular case. If a high number of combinations leads to satisfying results, a fine-tuning process does not have to be applied and the model seems more probable.

The calculations show that there is no substantial advantage of the knotted spectrum in reproducing the experimental values for masses and mixing. This is not a fail of the model but relies in the fact that the Dirac masses are treated as being totally free parameters in the numeric calculations. The claim that a degeneracy of the Dirac masses would arise automatically by fitting to the knotted spectrum cannot be hold. Therefore a mechanism to generate these nearly degenerated Dirac masses, e.g. an approximative or slightly broken symmetry, has to be found. In that case the analytic arguments would apply and can lead to an improved model where the knotted spectrum perform better than the random spectrum. If such a mechanism is found, the degeneracy of the Dirac masses has to be implemented into the computer code. With this assumption, a large difference between the knotted and the random spectrum is expected.

Chapter 4

Knotted Inflation

The derivations in this section with general aspects of cosmology are based on on [22].

The purpose of cosmology is to explain the evolution of the universe with laws of physics we already know. It is a mixture of general relativity, particle physics and thermodynamics and covers a broad field of physical effects. The model that describes the visible universe is called the Standard Model of cosmology, which is mostly accepted in the current research community.

4.1 Standard Model of Cosmology

In general relativity the metric describes the behavior of space time in the universe. Based on observations of a very isotropic universe and the well motivated assumption that the earth is in no sense special according to its position in space, it is reasonable to assume a homogeneous and isotropic space time. In the case of three spatial and one temporal dimension this space time can always be described by the Robertson-Walker metric in spherical coordinates

$$ds^2 = dt^2 - a^2(t)\left[\frac{dr^2}{1-kr^2} - r^2 d\Omega\right]. \tag{4.1}$$

Here $a(t)$ denotes the time dependent scale factor. The parameter k describes the space curvature:

$$k = \begin{cases} +1 \text{ spherical} \\ -1 \text{ hyperspherical} \\ 0 \text{ Euclidean} \end{cases} \tag{4.2}$$

The Einstein equations describe the evolution of space time in dependence on the energy content of the universe given by the energy momentum tensor $T_{\mu\nu}$

$$R_{\mu\nu} - \frac{1}{2} g_{\mu\nu} R = 8\pi G T_{\mu\nu}, \tag{4.3}$$

with the Ricci tensor $R_{\mu\nu}$, the Ricci scalar R and the Newton constant G. Using the Robertson-Walker metric (4.1) and a homogeneous and isotropic energy momentum tensor we get the two Friedmann equations

$$\dot{a}^2 + k = \frac{8\pi G\rho a^2}{3}, \tag{4.4}$$

$$\dot{\rho} = -\frac{2\dot{a}}{a}(\rho + p), \tag{4.5}$$

with the energy-density ρ and the pressure p. Equation (4.5) also accounts for energy-momentum conservation.

Obviously this leads to different behavior of the scale-factor $a(t)$ and therefore of the expansion of the universe for different relations between p and ρ. These relations depend on the type of energy-content:

$$\text{cold matter (e.g. dust): } p_M = 0 \rightarrow \rho_M \propto a^{-3}, \tag{4.6}$$

$$\text{hot matter (e.g. radiation): } p_R = \frac{\rho_R}{3} \rightarrow \rho_R \propto a^{-4}, \tag{4.7}$$

$$\text{vacuum energy: } p_V = -\rho_V \rightarrow \rho_V = const. \tag{4.8}$$

For a rough estimate of the behavior of the scale-factor in the early universe (small a), one can neglect the curvature-factor k in equation (4.4). This leads to

$$\text{cold matter: } a(t) \propto t^{\frac{2}{3}}, \tag{4.9}$$

$$\text{hot matter: } a(t) \propto t^{\frac{1}{2}}, \tag{4.10}$$

$$\text{vacuum energy: } a(t) \propto e^{\sqrt{\frac{\Lambda}{3}}t}, \tag{4.11}$$

with $\Lambda = 3\pi G\rho_V$. This allows to calculate the "'age" of the universe depending on the dominant energy content.

Assuming a mixture of different types of energy-content in the universe and also an arbitrary curvature k, it can be shown that the energy density yields

$$\rho = \frac{3H_0^2}{8\pi G}\left[\Omega_\Lambda + \Omega_M\left(\frac{a_0}{a}\right)^3 + \Omega_R\left(\frac{a_0}{a}\right)^4\right], \tag{4.12}$$

where the subscript 0 denotes the the present value. $H(t) = \frac{\dot{a}(t)}{a(t)}$ is the Hubble parameter, and Ω_i is defined by

$$\Omega_\Lambda = \frac{8\pi G}{3H_0^2}\rho_{V0}, \tag{4.13}$$

$$\Omega_M = \frac{8\pi G}{3H_0^2}\rho_{M0}, \tag{4.14}$$

$$\Omega_R = \frac{8\pi G}{3H_0^2}\rho_{R0}. \tag{4.15}$$

With equation (4.4) it follows that

$$\Omega_\Lambda + \Omega_R + \Omega_k = 1 \quad \text{and} \quad \Omega_k = -\frac{k}{a_0^2 H_0^2}. \tag{4.16}$$

4.2 Motivation for an era of Inflation

The common picture of the early universe is the so called hot Big Bang scenario, in which the universe starts in a state of extremely high temperature and density. During the first seconds after the Big Bang the universe is dominated by radiation and therefore expands according to (4.10). The expansion leads to a cool down of matter until nucleosynthesis takes place and cold matter dominated the expansion, see (4.9). Even though it is called cold matter, the particles still have enough energy to prevent recombination of the light nuclei with electrons. This is caused by photon scattering in the very dense universe. Only after the universe has expanded and consequently cooled down enough, the electrons and nuclei recombine to atoms and the universe becomes transparent. At that time the cosmic microwave background (CMB) originates. Caused by the redshift of the still expanding universe, nowadays one can see the radiation from the time of recombination in the microwave spectrum. The temperature of the CMB is measured to $T_{CMB} = 2.72548 \pm 0.00057$ K and is isotropic up to a deviation of $\frac{\Delta T}{T} = 10^{-4}$ [23]. The CMB is the earliest measurable relic of the universe based on electro-magnetic radiation. A measurement of a cosmic neutrino background could yield direct information of the time before recombination but is far out of reach of present experiments.

The assumption of a hot Big Bang in which all the energy was located at one single point leads to three major problems which may be solved by a phase of inflationary expansion:

- Problem of flatness: Observations of supernova redshift and CMB-fluctuations favor $\Omega_k = 0$ but still give room for a small $|\Omega_k| < 1$. According to Equation (4.16), Ω_k changes with $\dot{a}^{-2}$. Therefore Ω_k increases in matter- and radiation-dominated phases. If Ω_k is small and nonzero today, which corresponds to a nearly flat universe, Ω_k has to be even smaller at the time of the Big Bang leading to an even flatter universe. This is not ruled out but seems unnatural. An attractive solution is a period of inflation with dominating vacuum-energy, so that $\dot{a}/a$ is constant as in equation (4.11). Then Ω_k decreases with a^{-2} and an arbitrary curvature Ω_k at the beginning of the inflationary period would automatically lead to an extremely flat universe.

- Problem of horizons: As mentioned above the CMB temperature is extremely isotropic. This leads to the horizon problem. It can be shown that the horizon was about 1.6° during the first emergence of the CMB. Therefore one would expect no physical relations between regions which are outside this horizon. Inhomogeneities could not have been smoothed out over such a big region as suggested by the CMB. Again, an age of inflationary expansion before the time of radiation domination can solve this problem. All of the visible universe was confined to a tiny region before inflation, in which it easily could have been homogeneous.

- Problem of monopoles: Several theories such as grand unified theories predicts monopoles as relics after symmetry breaking. Rough estimates favor a similar amount of monopoles and nuclei but there is no evidence for even a single observed

monopole. An inflationary phase occurring after the production of the monopoles but before the production of the nuclei would lead to a much reduced expected number of monopoles.

The most striking reason for cosmological inflation is the formation of structure. The structure in the universe is scale invariant and can be explained by inflation via quantum mechanical perturbations. These perturbations are seeds for structure formation and occur during the era of inflation. This leads to similar structures on different scales.

Several models with an inflationary phase have been proposed in the last years. A way to motivate a specific model of inflation by experimental data (or at least the possibility to falsify it) is the observation of B-modes in the CMB. Gravitational waves as relics of the inflation would polarize the CMB in a special way so that B-modes arise. First evidence of such B-modes was reported by BICEP2 in 2014 [24]. A current analysis by PLANCK suggests that the dust foreground may be underestimated in the BICEP2 analysis [25]. A joint analysis of both experiments is announced.

One problem of inflation models is the source of the vacuum energy. A proposed scalar Inflaton field in a state of high energy can represent the vacuum energy. The approach of [26] to realize such a vacuum energy is taken as a basis in this thesis.

4.3 Knotted Inflation

As seen in chapter 2.3, it is possible to form flux tubes in (non-) Abelian gauge theories like grand unified theories. Assuming such a theory with a Landau-Ginzburg Lagrangian (2.3) (for instance confinement in QCD), a network of flux tubes can arise after the phase transition. It is likely that the flux tubes are not separated but form a highly knotted network. Each flux tube with radius a carries the quantized chromoelectric flux Φ and therefore can be described by a constant chromoelectric field

$$E_i = F_{0i} = \frac{\Phi}{\pi a^2} n_i, \tag{4.17}$$

with the vector n_i orthogonal to the flux tube section. The entire network will then give rise to a non vanishing vacuum energy density given by

$$\rho_E = \frac{1}{2}|\vec{E}|^2 = \frac{1}{2}\frac{Tr\Phi^2}{(\pi a)^2}. \tag{4.18}$$

The network is assumed to be roughly stable in three dimensions since loosening this network corresponds to breaking the strings. In more than three dimensions, knots can always be loosened (see chapter 2.1) and therefore a knotted network will not arise which leads to no period of nearly stable vacuum energy. This can explain why there are exact three spatial dimensions, since otherwise no inflation takes place.

This now produced constant energy density corresponds to the vacuum energy of an inflationary era. Since string-breaking of the flux tubes is unlikely but still possible due to quantum-tunneling-processes, the network will slowly decay. As long as the

network is large enough and covers the whole universe, the energy density decreases slowly enough to ensure inflation. Only after the network decayed into too small parts the inflation will end. This corresponds exactly to the phase transition in a "backward" percolation process.

This part of the thesis is about simulating this decay of the network to find out whether in the model of knotted inflation a phase transition takes place after an era of inflation.

4.4 Percolation Theory

Percolation theory describes the formation of infinitely large clusters in a given topology, where linkings between different points occur randomly. Let us assume an infinitely large lattice where two lattice points, the sites, next to each other are either connected or not, denoted by the probability p. Two or more connected sites built up a so called cluster. It can be shown that a critical probability p_c exists, so that an infinitely large cluster exist for $p > p_c$. For regularly shaped lattices p_c can be determined analytically but for arbitrary topologies simulations with a finite sized lattice have to be used. (see [27] for a review).

To describe a knotted inflation we want to determine p_c by starting with a percolated network. This network is generated by the mechanism introduced above. The closed flux tubes are knotted with other flux tubes, which is interpreted as a connection in the percolation-picture. At the beginning every flux tube is considered to be highly knotted and the whole network consists of just one big cluster. After that each flux tube can decay with a probability of p_{dec} leading to a steady decrease of connections. If a critical number of connections is reached, we expect a phase transition at which the infinitely large cluster decays, corresponding to an end of percolation due to an undercritical connection probability. Since a simulation of an infinite network is not possible we reduce to a finite number of knotted flux tubes and the phase transition is then determined by a substantial decrease of the size of the biggest cluster in the network.

The following section will introduce a simulation of such a decay process for two different topologies.

4.5 Simulating Inflation via Knotted Networks

4.5.1 Basic concepts of the simulations

The simulation is coded as an object oriented C++-program. The closed flux tubes introduced above are treated as an object of the custom class "tube". To get access to the flux tubes each object has a list of pointers to the tubes it is linked with. Therefore it is easy to address the linked flux tubes if one tube decays.

The program consists of three different parts. The first part contains the creation of the network in which all objects are initialized and the structure of the network

is determined by specifying the list of linked tubes. We will have a closer look at two different structures, see sections 4.5.3 and 4.5.4. After the creation, the network dynamics are simulated stepwise in a loop. In each loop repetition the second and third part are done one after another. The second part simulates the decay of the single flux tubes. Each tube is terminated with the probability p_{dec}, which can be adjusted arbitrarily. If a tube is terminated this object has to be deleted from the list of linked tubes so that addressing tubes still works. After that decay, the third part of the program calculates the number of clusters as well as the number of tubes in the biggest cluster. This is done using the Hoshen-Kopelman-Algorithm, see 4.5.2. These numbers are written into the output file for interpreting the results. Each step in the loop corresponds to a time unit and defines the time scale. By adjusting the probability p_{dec} one can adjust the average number of decaying tubes and therefore obtain a higher time resolution by decreasing p_{dec}. To ensure a realistic behavior, the total number of tubes has to be large enough.

4.5.2 Hoshen-Kopelman Algorithm

The Hoshen-Kopelman algorithm was developed by J. Hoshen and R. Kopelman in 1976 [28]. It is an algorithm to identify and label all clusters in a given structure. The algorithm determines a label (integer numbers) for each site which states the cluster it belongs to. Sites with the same label belong to the same cluster. To label the entire structure the algorithm scans the structure site by site. If a site is not occupied the algorithm skips to the next site. If it is occupied, the algorithm searches for neighbors which were labeled before. If there are none, the site receives a new label, which has not been used before. If there are labeled neighbors, the site receives the smallest label of the neighbors. The higher label get a remark in an additional vector, that these labels belong to the same cluster. The output of the algorithm is the labeled structure and a vector, in which the cluster size for each label is denoted, making it a useful tool for identifying clusters and cluster sizes.

4.5.3 Lattice Network

An easy approach to build a linked network is to place the tubes on a three dimensional lattice. We assume each tube to be a ring that is initially connected to exactly four other tubes, which are located above and beneath, right and left or behind and in front. For a better understanding, Figure 4.1 shows the linkings of one single tube. This pattern can be repeated all over the lattice. Because of the three possible orientations of the tubes, a three dimensional lattice develops where not all lattice sites are occupied.

To apply the Hoshen Kopelman-Algorithm, we used the implementation by T. Fricke [29] and expanded it to a three dimensional lattice. Periodic boundary conditions are implemented for a better simulation of an infinite structure.

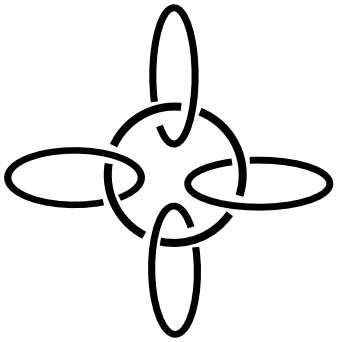

Figure 4.1: Scheme of linkings in the cubed network

4.5.4 Random network

For a more realistic scenario we developed a randomly linked network, for which we have to adjust the initialization process. We initialized one tube after the other, and every new initialized tube is linked it to all the other previous produced tubes with a probability p_{link}. Since the randomly linked network does not rely on a specific structure of the tubes at the time of formation, it is more realistic than the previous case. By adjusting the linking probability p_{link}, one adjusts the average number of tubes one tube is linked to.

We applied the Hoshen-Kopelman-Algorithm to that randomly linked network by simply scrolling through the whole list of tubes instead of using an underlying lattice structure.

4.6 Results

The figures 4.2, 4.3, 4.4 and 4.5 show the results of the simulations described above. While figure 4.5 refers to the lattice network the figures 4.2, 4.3 and 4.4 refer to the random network with the different values of p_{link} so that the average number of linkings for each flux tube at the start of the simulation is determined to 5, 10 and 100. The random networks consist of 10,000 flux tubes and the decay probability is set to $p_{decay} = 1\%$. Since the simulation for the lattice network needs less computing time the total number of tubes is set to 750,000 and the decay probability is set to $p_{decay} = 0.01\%$ to achieve a higher time resolution.

The basis of every plot is the simulation of a decaying network which is repeated ten times. After that the calculated values are averaged. This is done to avoid fluctuations and to smooth the plots. The horizontal axis of each plot corresponds to the steps of the decay process and therefore can be interpreted as a time scale. The vertical axis simply denotes the number of the different derived quantities in the network in a logarithmic scale.

The total number of remaining flux tubes is shown in turquoise dots. As expected,

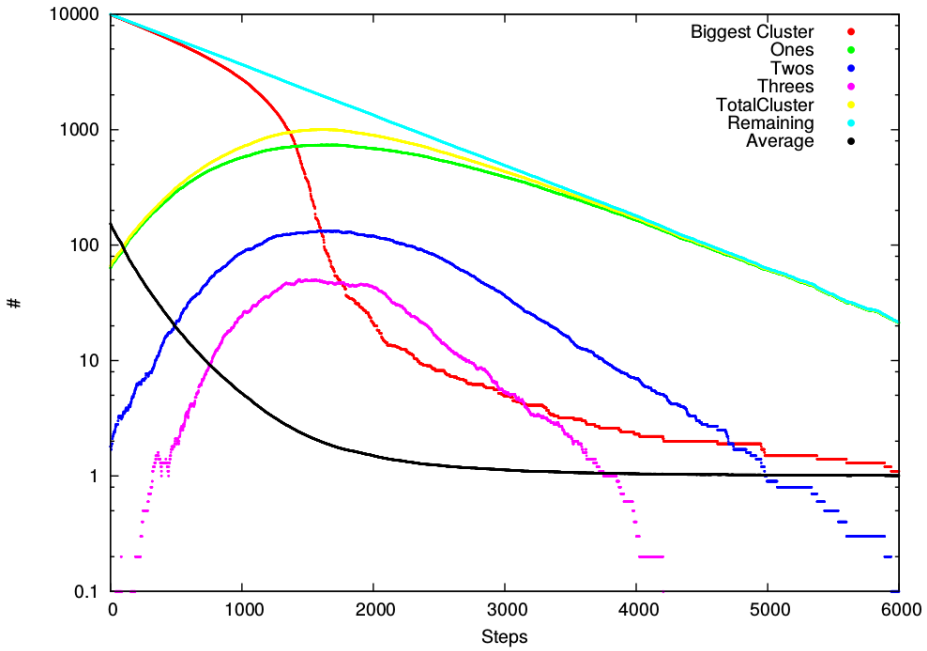

Figure 4.2: Result of Simulation of a random network with a total number of 10,000 tubes and an average of 5 linkings at beginning.

the total number decreases exponentially.

The dots in green correspond to the number of single unlinked tubes. The blue and violet dots correspond to the number of the two smallest possible clusters consisting of two and three flux tubes, respectively. The quantity of these small clusters starts at zero for the highly linked random networks. This was expected, since a high linking probability will not lead to separated flux tubes in the beginning. Only the random network, which starts with an average number of linkings of 5 leads to a few of these small clusters in the beginning of the simulation. Obviously these small clusters do not exist in the lattice network since the initial setup only provides one big cluster. In general the number of these small clusters ascend at the first time because more and more small parts separate from the bigger clusters. This formation of small clusters dominate over the decay of the already existing small clusters. The domination will not hold any more if the bigger clusters become too small. Then the decay of small clusters will be the main effect and the number of those small clusters will descend.

The yellow dots donate the total number of clusters. For the highly linked networks and the lattice network this number obviously starts at 1 because only one big cluster

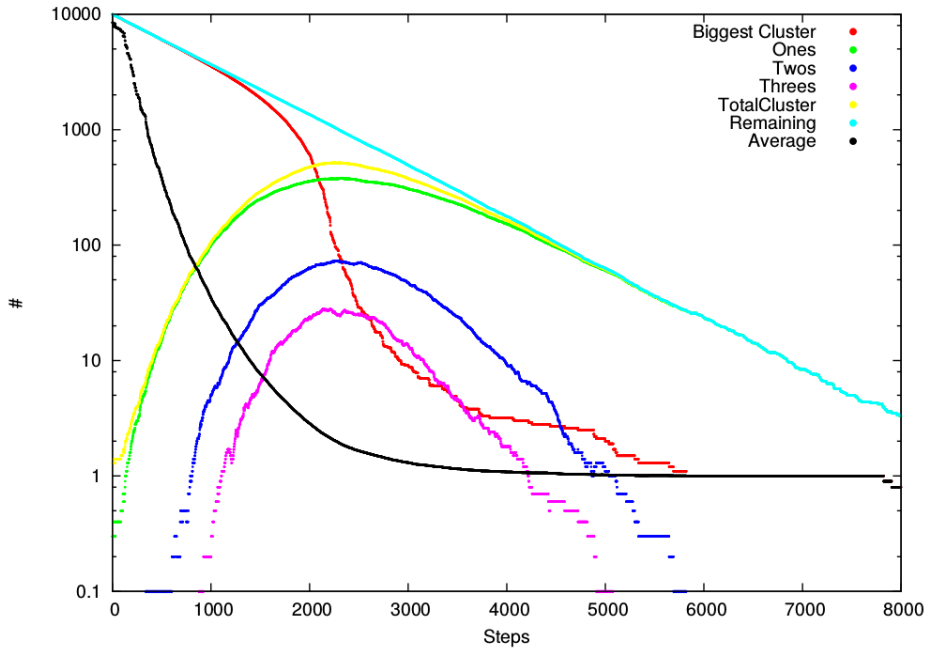

Figure 4.3: Result of Simulation of a random network with a total number of 10,000 tubes and an average of 10 linkings at beginning.

is produced initially.

For a larger number of steps, which corresponds to later times, the total number of clusters, the number of single flux tubes and the total number of remaining flux tubes will be the same. That corresponds to totally separated flux tubes without any linking.

The black dots show the average cluster size. For the highly linked random network and the lattice network the average cluster size starts at the total number of flux tubes because there is only one big cluster. When the first separated clusters arise, the average cluster size decreases faster than before until it ends up at one single tube, where only unlinked flux tubes exist in the network.

The most interesting value is shown in red and denotes the size of the biggest cluster. This is the number of flux tubes which belong to the biggest cluster. At the first part of the decay process, the size of the biggest cluster declines with the expected decay rate just like the total number of remaining flux tubes. This era corresponds to the era of inflation. The breakdown of the network can be clearly seen, when the size of the biggest cluster decreases stronger than before. This corresponds to an end of inflation. The duration of inflation can be adjusted by the two parameters p_{link} and p_{decay}, while

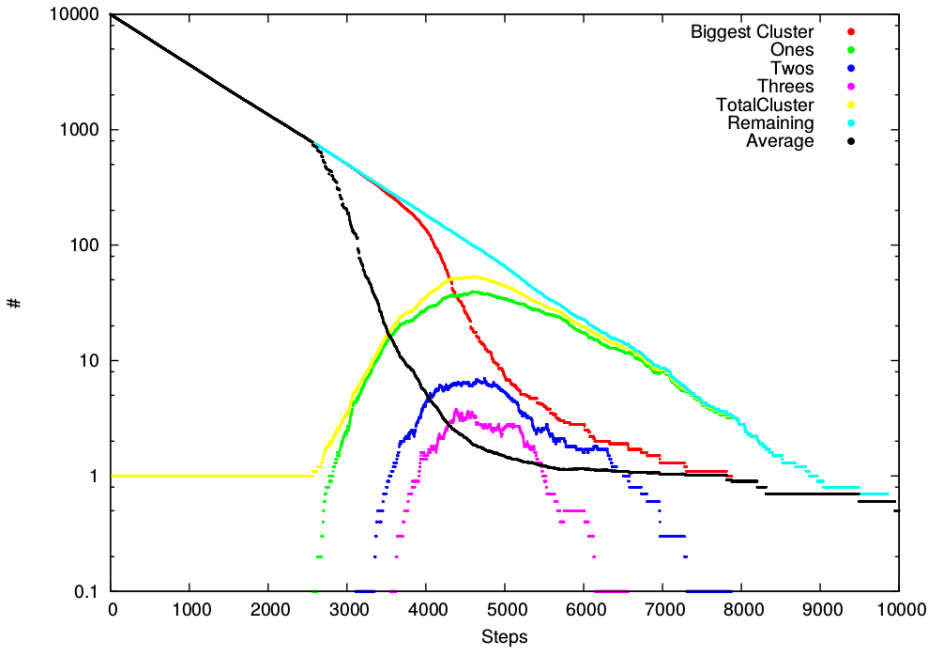

Figure 4.4: Result of Simulation of a random network with a total number of 10,000 tubes and an average of 100 linkings at beginning.

the decay probability p_{decay} only shifts the time scale. The linking probability is related to the duration of inflation since a higher linking needs more flux tubes to decay so that the entire network will collapse. For a comparison figure 4.6 shows the size of the biggest cluster for the three different linking setups in the case of a random network.

By comparing the lattice network with the randomly knotted network one can see the difference caused by the lower average number of linkings, which is determined to four in the case of the lattice network. Since the number of linkings is small, one would not expect all flux tubes to belong to the biggest cluster in case of a random network. The special structure used in the lattice network automatically considers only flux tubes belonging to the initial cluster. These are the only ones contributing to inflation. Additionally the decay process of the biggest cluster looks the same no matter of using a random or lattice network. Therefore a simulation of a network based on a lattice like structure such as used here is recommended. The required computing time is much lower and the simulation does not lead to extremely different results.

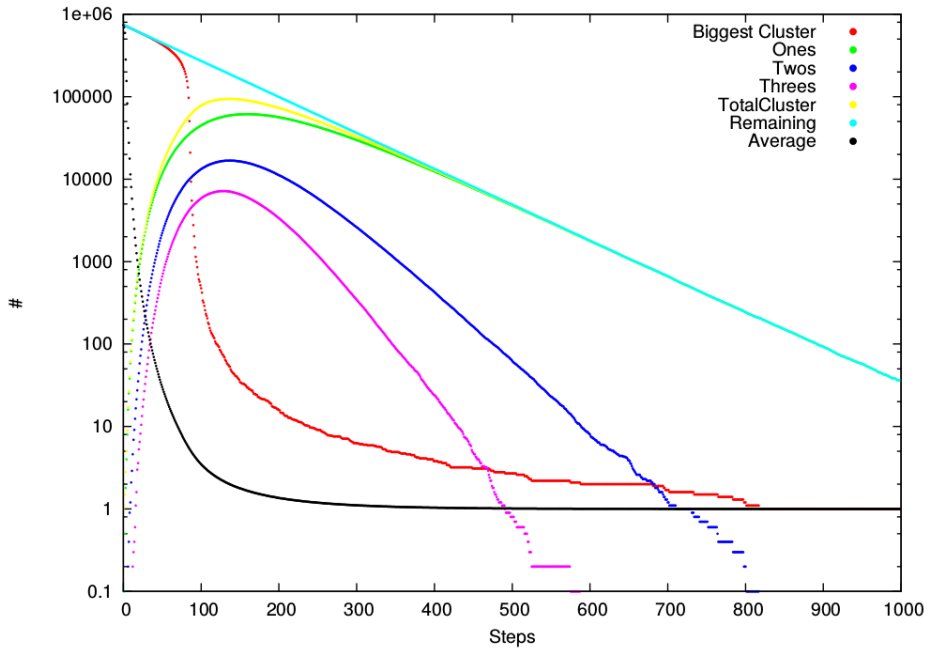

Figure 4.5: Result of simulation of a lattice network.

4.7 Interpretation

The simulations show that a phase transition takes place in a knotted network. Therefore the model of a knotted inflation leads to the proposed era of inflation and as well indicates an end of inflation. To obtain more concrete implications of such scenarios the underlying physics has to be understood and modeled more thoroughly. The probability of building those closed flux tubes is not determined by now as well as the probability that these flux tubes are linked to each other. It seems obvious that it will be a highly complex mechanism depending on properties such as the temperature, the density and the pressure at the time of phase transition of the gauge theory. As well it is not clear at the current point of research if the developing flux tubes repel each other. If this is not the case no network will evolve. If this all applies, one also has to check whether such a simulated phase transition can be calculated analytically and if cosmological properties such as critical exponents can be determined.

While the idea of knotted inflation looks attractive and promising, much work remains to be invested in order to develop a quantitative and testable model.

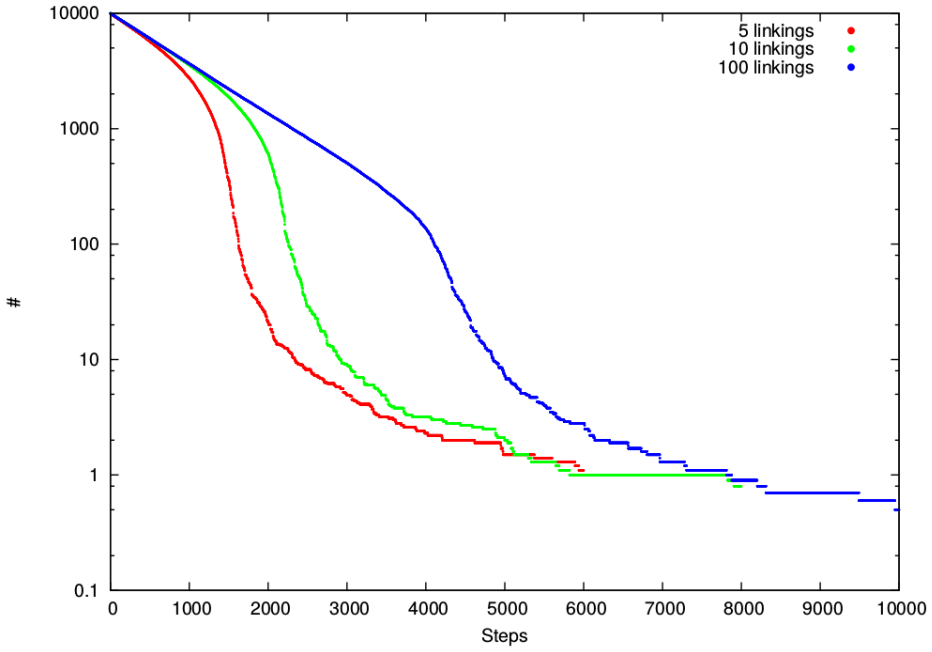

Figure 4.6: Comparison of random networks.

Chapter 5

Conclusion & Outlook

Until now topologically motivated models in the area of phenomenological high energy physics did not attract much interest even if there are promising realizations of tightly knotted and linked flux tubes in context of phenomenology, e.g. Glueballs [30].

This thesis analyzed two different ideas to apply string like objects which arise as flux tubes after a phase transition in a Landau-Ginzburg model.

The first one was considered to give a hint of the origin of the neutrino masses and the characteristic of large mixing angles in the lepton sector. We used a Seesaw Type I mechanism and adopted values for the right handed neutrino mass matrix with values determined by the knotlengths. Assuming a diagonal Dirac mass matrix, these entries were fitted to reproduce the experimental values of mixing and mass squared differences of the neutrinos. A significant difference between a knotted and a random spectrum can not be seen. The analytical assumption of degeneracy in the Dirac mass matrix needs to be an input into the numerical calculations otherwise a knotted model is not favored. A search for a mechanism to create such degeneracy can be seen as a starting point for further research where afterwards the numerical calculations as well can be adjusted and a difference between the knotted and the random spectrum is expected.

The second model we looked at was a simulation of a knotted inflation. In this model cosmological inflation is triggered by a network of highly linked flux tubes. These linkings slowly decay caused by quantum fluctuations and tunneling processes. In the simulations we found the expected phase transition at which the network collapses and inflation will end. This corresponds to a backward percolation process. In general percolation emerges in various processes in different areas of science including computer science, biology or social science as well as in physics, e.g. solid state physics. It is a good example for applying a theoretical idea to a wide field of interest. In the case of knotted inflation the underlying mechanism of inflation has to be studied more thoroughly to obtain quantitative results and predictions.

In general, non trivial topologies show a lot of interesting features and a closer look at these properties might be motivated by unsolved problems in the context of high energy physics.

Appendix A

Numeric calculations for comparison with former analysis

The experimental values used in [17] for this comparison are given by [31]

$$\theta_{12} = 34.4 \pm 1.0\ ^\circ \tag{A.1}$$
$$\theta_{23} = 42.8^{+4.7}_{-2.9}\ ^\circ \tag{A.2}$$
$$\theta_{13} = 5.6^{+3.0}_{-2.7}\ ^\circ \tag{A.3}$$
$$\delta m^2_{21} = 7.59 \pm 0.2 \cdot 10^{-5}\text{eV}^2 \tag{A.4}$$
$$\delta m^2_{31} = -2.36 \pm 0.11 \cdot 10^{-3}\text{eV}^2 \text{ (IH)} \tag{A.5}$$
$$\delta m^2_{31} = 2.46 \pm 0.12 \cdot 10^{-3}\text{eV}^2 \text{ (NH)} \tag{A.6}$$

χ^2	K_1	K_2	K_3	L_1	L_2	L_3	m_1^D[GeV]	m_2^D[GeV]	m_3^D[GeV]
< 0.001	00	01	04	10	16	12	7.945	28.911	21.765
< 0.001	00	01	04	11	06	10	7.975	29.134	21.835
< 0.001	00	01	04	11	16	10	7.968	29.139	21.789
< 0.001	00	01	04	17	05	11	8.032	29.432	22.080
< 0.001	00	01	04	17	07	11	8.019	29.442	21.997
< 0.001	00	07	12	08	06	05	5.774	14.179	22.629
< 0.001	00	07	12	08	16	05	5.769	14.178	22.574
< 0.001	01	05	04	13	06	12	6.820	21.487	15.609
< 0.001	01	06	04	16	11	08	7.537	16.000	24.961
< 0.001	02	03	11	11	17	10	7.250	20.027	16.859
< 0.001	02	07	05	11	07	09	5.862	16.946	12.434

Table A.1: The 10 best fits for normal hierarchy

χ^2	K_1	K_2	K_3	L_1	L_2	L_3	m_1^D[GeV]	m_2^D[GeV]	m_3^D[GeV]
< 0.001	00	09	02	07	17	03	72.58	-9.823	7.843
< 0.001	00	09	02	07	17	03	72.390	9.799	7.824
< 0.001	00	11	09	08	07	09	42.154	7.298	6.701
< 0.001	01	11	08	11	04	09	44.515	6.920	6.334
< 0.001	01	13	03	12	02	04	43.693	6.819	5.477
< 0.001	04	09	07	00	08	09	65.649	15.465	14.108
< 0.001	04	11	12	06	08	17	40.423	7.033	6.523
< 0.001	04	12	11	05	08	17	40.038	7.053	6.499
< 0.001	05	11	13	06	02	17	41.961	7.458	6.914
< 0.001	06	10	12	06	08	11	41.673	7.173	6.708
< 0.001	06	12	11	08	06	17	40.691	7.045	6.504

Table A.2: The 10 best fits for inverse hierarchy

Model	tested parameters	viable fits	ratio viable fits	$\chi^2_{bestfit}$
NHknots	10,692,864	271,599	2.72%	< 0.001
NHrandom	1,000,000	27,390	2.74%	< 0.001
IHknots	10,692,864	253,956	2.38%	< 0.001
IHrandom	1,000,000	9,208	0.92%	< 0.001

Table A.3: Number of viable fits for the different models

Danksagung

Zu aller erst bedanke ich mich bei dem Betreuer meiner Masterarbeit, Prof. Heinrich Päs für die vielen Ratschläge und immer neuen Ideen. Vor allem aber für die Motivation in den Phasen, in denen sie mir fehlte. Vielen Dank auch für die Möglichkeit an der DPG Frühjahrstagung und am DESY-Theorie Workshop teilnehmen zu können.

Ein ganz großes Dankeschön geht an den gesamten vierten Stock. Ihr habt mich sofort herzlich aufgenommen, und ich habe mich von Anfang an wohl gefühlt. Während der ganzen Masterarbeit bin ich gerne ins Büro gekommen, was vor allem an dem tollen Arbeitsklima liegt. Ihr alle seid immer offen für Fragen, sei es fachlicher oder privater Natur. Wir hatten viele erhellende Diskussionen, die mir immer Spaß gemacht haben. Ich bin sicher, das wird auch weiterhin so sein und freue mich schon auf die Zeit während meiner Promotion. Everyone is awesome!

Für das Korrekturlesen und die sehr hilfreichen Anmerkungen haben sich Erik und Peter einen extra Dank erarbeitet. Vielen Dank!

Natürlich danke ich auch all meinen Freunden, die mir zu den passenden Zeiten die nötige Ablenkung beschert haben und mir vor allem immer dann zur Seite standen, wenn ich sie gebraucht habe. Gute Freunde erkennt man daran, dass sie nicht vor drastischen Worten zurück schrecken, wenn sie gebraucht werden. Danke.

Zuletzt gebührt mein Dank meiner Familie. Die letzte Zeit war für uns alle sehr turbulent und nicht immer schön. Ich danke euch für eure Unterstützung und dass ihr mir immer den Rücken frei gehalten habt, auch wenn es für euch nicht immer einfach war. Gerade im letzten Monat konnte ich nicht so für euch da sein, wie ich es mir gewünscht hätte. Danke für euer Verständnis.

Mir hat das letzte Jahr sehr viel Spaß gemacht und es war sicherlich das schönste Jahr meines Studiums. Ich freue mich auf die kommenden Herausforderungen während meiner Promotion und bin sehr glücklich, dass ihr alle an meiner Seite steht.

List of References

[1] Michael E. Peskin and Dan V. Schroeder. *An Introduction To Quantum Field Theory (Frontiers in Physics)*. Westview Press, 1995.

[2] M. Fukugita and T. Yanagida. *Physics of neutrinos and applications to astrophysics*. Springer, 2003.

[3] Gudrun Hiller and Heinrich Päs. Lecture notes on "flavor theory", given in summer 2014. Lecture notes, given in Summer 2014.

[4] Nicola Cabibbo. Unitary Symmetry and Leptonic Decays. *Phys.Rev.Lett.*, 10:531–533, 1963.

[5] Makoto Kobayashi and Toshihide Maskawa. CP Violation in the Renormalizable Theory of Weak Interaction. *Prog. Theor. Phys.*, 49:652–657, 1973.

[6] L. Wolfenstein. Parametrization of the Kobayashi-Maskawa Matrix. *Physical Review Letters*, 51:1945–1947, November 1983.

[7] C. Weinheimer, B. Degen, A. Bleile, J. Bonn, L. Bornschein, et al. High precision measurement of the tritium beta spectrum near its endpoint and upper limit on the neutrino mass. *Phys.Lett.*, B460:219–226, 1999.

[8] V.N. Aseev et al. An upper limit on electron antineutrino mass from Troitsk experiment. *Phys.Rev.*, D84:112003, 2011.

[9] M. Agostini et al. Results on Neutrinoless Double-β Decay of ^{76}Ge from Phase I of the GERDA Experiment. *Phys.Rev.Lett.*, 111(12):122503, 2013.

[10] P.A.R. Ade et al. Planck 2013 results. I. Overview of products and scientific results. 2013.

[11] M.C. Gonzalez-Garcia, Michele Maltoni, Jordi Salvado, and Thomas Schwetz. Global fit to three neutrino mixing: critical look at present precision. *JHEP*, 1212:123, 2012.

[12] kismalac. Neutrino hierarchies. Published via Wikimedia Commons under creative commons license.

[13] Richard H. Crowell and Ralph H. Ralph Hartzler Fox. *Introduction to knot theory.* Graduate texts in mathematics. Springer-Verlag, [1977] c1963, New York, 1963. Includes index.

[14] T. Ashton, J. Cantarella, M. Piatek, and E. Rawdon. Knot Tightening By Constrained Gradient Descent. *ArXiv e-prints*, February 2010.

[15] Georges Ripka. Dual superconductor models of color confinement. 2003.

[16] Philipp Leser and Heinrich Päs. Neutrino mass hierarchy and the origin of leptonic flavor mixing from the righthanded sector. *Phys.Rev.*, D84:017303, 2011.

[17] Thomas W. Kephart, Philipp Leser, and Heinrich Päs. Knotted strings and leptonic flavor structure. *Mod.Phys.Lett.*, A27:1250224, 2012.

[18] P.F. Harrison and W.G. Scott. Permutation symmetry, tri - bimaximal neutrino mixing and the S3 group characters. *Phys.Lett.*, B557:76, 2003.

[19] Brian Gough. *GNU Scientific Library Reference Manual - Third Edition.* Network Theory Ltd., 3rd edition, 2009.

[20] R. Barlow. Asymmetric Errors. *ArXiv Physics e-prints*, January 2004.

[21] J. A. Nelder and R. Mead. A simplex method for function minimization. *Computer Journal*, 7:308–313, 1965.

[22] S. Weinberg. *Cosmology.* Cosmology. OUP Oxford, 2008.

[23] D. J. Fixsen. The Temperature of the Cosmic Microwave Background. *apj*, 707:916–920, December 2009.

[24] P.A.R. Ade et al. Detection of B-Mode Polarization at Degree Angular Scales by BICEP2. *Phys.Rev.Lett.*, 112:241101, 2014.

[25] R. Adam et al. Planck intermediate results. XXX. The angular power spectrum of polarized dust emission at intermediate and high Galactic latitudes. 2014.

[26] A. Berera, R. Bunyi, T. Kephart, H. Päs, and J. Rosa. Notes on knotted inflation, to be published.

[27] J W Essam. Percolation theory. *Reports on Progress in Physics*, 43(7):833, 1980.

[28] J. Hoshen and R. Kopelman. Percolation and cluster distribution. i. cluster multiple labeling technique and critical concentration algorithm. *Phys. Rev. B*, 14:3438–3445, Oct 1976.

[29] T. Fricke. Implementation of hoshen-kopelman algorithm in c. `https://www.ocf.berkeley.edu/~fricke/projects/hoshenkopelman/hoshenkopelman.html`, September 2014.

[30] Roman V. Buniy and Thomas W. Kephart. A Model of glueballs. *Phys.Lett.*, B576:127–134, 2003.

[31] M.C. Gonzalez-Garcia, Michele Maltoni, and Jordi Salvado. Updated global fit to three neutrino mixing: status of the hints of $\theta_{13} > 0$. *JHEP*, 1004:056, 2010.

Eidesstattliche Versicherung

Ich versichere hiermit an Eides statt, dass ich die vorliegende Masterarbeit mit dem Titel "Knots and Links in High Energy Physics" selbständig und ohne unzulässige fremde Hilfe erbracht habe. Ich habe keine anderen als die angegebenen Quellen und Hilfsmittel benutzt sowie wörtliche und sinngemäße Zitate kenntlich gemacht. Die Arbeit hat in gleicher oder ähnlicher Form noch keiner Prüfungsbehörde vorgelegen.

Ort, Datum | Unterschrift

Belehrung

Wer vorsätzlich gegen eine die Täuschung über Prüfungsleistungen betreffende Regelung einer Hochschulprüfungsordnung verstößt handelt ordnungswidrig. Die Ordnungswidrigkeit kann mit einer Geldbuße von bis zu 50.000,00 € geahndet werden. Zuständige Verwaltungsbehörde für die Verfolgung und Ahndung von Ordnungswidrigkeiten ist der Kanzler/die Kanzlerin der Technischen Universität Dortmund. Im Falle eines mehrfachen oder sonstigen schwerwiegenden Täuschungsversuches kann der Prüfling zudem exmatrikuliert werden (§ 63 Abs. 5 Hochschulgesetz - HG -).

Die Abgabe einer falschen Versicherung an Eides statt wird mit Freiheitsstrafe bis zu 3 Jahren oder mit Geldstrafe bestraft.

Die Technische Universität Dortmund wird ggf. elektronische Vergleichswerkzeuge (wie z.B. die Software "turnitin") zur Überprüfung von Ordnungswidrigkeiten in Prüfungsverfahren nutzen.

Die oben stehende Belehrung habe ich zur Kenntnis genommen.

Ort, Datum | Unterschrift